Review of Scientific Instruments

Design and development of an automated experimental setup for ion transport measurements

Cite as: Rev. Sci. Instrum. **93**, 064104 (2022); https://doi.org/10.1063/5.0086296
Submitted: 24 January 2022 • Accepted: 21 May 2022 • Published Online: 08 June 2022

Sharad Kumar Yadav, Mukesh Kumar, Sundara Ramaprabhu, et al.

View Online
Export Citation
CrossMark

Review of Scientific Instruments
Special Issue: Advances in Measurements and Instrumentation Leveraging Embedded Systems
Read Now!

AIP Publishing

© 2022 Author(s).

Review of
Scientific Instruments
ARTICLE
scitation.org/journal/rsi

Design and development of an automated experimental setup for ion transport measurements

Cite as: Rev. Sci. Instrum. 93, 064104 (2022); doi: 10.1063/5.0086296
Submitted: 24 January 2022 • Accepted: 21 May 2022 •
Published Online: 8 June 2022

Sharad Kumar Yadav,[1,2,3] **Mukesh Kumar,**[2,3] **Sundara Ramaprabhu,**[2,4] **Vishal V. R. Nandigana,**[1,3] **and Pramoda K. Nayak**[2,3,5,a)]

AFFILIATIONS

[1] Department of Mechanical Engineering, Indian Institute of Technology Madras, Chennai 600036, India
[2] Department of Physics, Indian Institute of Technology Madras, Chennai 600 036, India
[3] Micro Nano and Bio-Fluidics Group, Indian Institute of Technology Madras, Chennai 600036, India
[4] Alternative Energy and Nanotechnology Laboratory (AENL), Nano Functional Materials Technology Centre (NFMTC), Indian Institute of Technology Madras, Chennai, India
[5] 2D Materials Research and Innovation Group, Indian Institute of Technology Madras, Chennai 600036, India

[a)] **Author to whom correspondence should be addressed:** pnayak@iitm.ac.in

ABSTRACT

The ion transport measurements using various ion-exchange membranes (IEMs) face several challenges, including controllability, reproducibility, reliability, and accuracy. This is due to the manual filling of the solutions in two different reservoirs in a typical diffusion cell experiment with a random flow rate, which results in the diffusion through the IEM even before turning on the data acquisition system as reported so far. Here, we report the design and development of an automated experimental setup for ion transport measurements using IEMs. The experimental setup has been calibrated and validated by performing ion transport measurements using a standard nanoporous polycarbonate membrane. We hope that the present work will provide a standard tool for realizing reliable ion transport measurements using ion-exchange membranes and can be extended to study other membranes of various pore densities, shapes, and sizes.

Published under an exclusive license by AIP Publishing. https://doi.org/10.1063/5.0086296

I. INTRODUCTION

Ion transport through ion-exchange membranes (IEMs) is crucial in electrochemical separation, energy scavenging, and energy storage units. The novel IEMs are vital in water desalination,[1] fuel cells,[2] redox flow cells,[3] pressure retarded osmosis,[4] and reverse electrodialysis.[5–7] These membranes are of different types, including polymer-based,[8–10] solid-state,[11–13] composites,[14–16] and lower dimension membranes, such as graphene[17,18] and MoS_2,[19–21] which show better ion selectivity, high surface charge density, and very high conductance.[19,20,22–24] The aforementioned remarkable properties of these membranes play a vital role in developing membrane-based technology, such as harvesting energy using a salinity gradient,[25,26] where the IEM allows either the cation or anion to pass (diffuse) through it, which results in an ionic current.[27,28]

There are various challenges in ion transport measurements, including controllability, reproducibility, reliability, and accuracy.[29] This is due to the manual filling of the solutions in the diffusion cells (housing the IEM) with some random flow rate (causes an initial pressure difference across the IEM), which results in the diffusion (ion/electrolyte) through the IEM even before turning on the data acquisition system as reported in the literature.[13,30–33] The manual filling[30,31,34–36] and the delay in data acquisition allow a change in the expected initial condition, leading to unreliable results. So, there is a need to maintain a constant difference in the concentration, viscosity, or density of the two solutions across the membrane. In addition, the manual operation causes a sufficient delay to realize the phenomenon such as the ion concentration polarization[37] (occurs when the concentration of a particular species enriches or depletes at the boundary layer close to the membrane surface due to the selective transport through the membrane) effect even before starting the measurement. Hence, an automated diffusion cell experimental setup along with data acquisition is very much needed to minimize the issues such as controllability, reproducibility, and accuracy and provide a reliable ion transport characteristic.

In the present work, we have designed and developed a complete automated experimental setup for the ion transport measurements using IEMs. This paper is organized as follows: Sec. II provides an overview of the experimental setup and all the assembled units. Section III presents the instrumentation and automation of the experimental assembly and data acquisition. Section IV demonstrates the calibration of components used in the experimental setup, followed by Sec. V, which deals with the ion transport measurement. This automated setup has validated the ion transport measurement using a standard nanoporous polycarbonate membrane. This work will provide a standard tool for realizing reliable ion transport measurements using IEMs, and this study can be extended to other membranes.

II. EXPERIMENTAL SETUP

The experimental setup is designed assembled to study ion transport through IEMs. Figure 1 shows the schematic of this experimental setup. The ions move through the IEMs either due to an external force (electric field, pressure, or temperature gradient) or the chemical potential between two solutions having a concentration,[31,38] viscosity,[35] or conductivity difference.[31,35,39–41] Hence, to develop the experimental setup for ion transport across IEMs, the two diffusion cells (containing solution-1 and solution-2 as in Fig. 1) are assembled, including the solutions having a concentration difference, viscosity difference, or different mix-solution. The chemical pumps CH-1 and CH-2 (KE100, KEMS magnetic centrifugal chemical pump) are used for pumping the solutions from the reservoir to the diffusion cells rapidly with a flow rate of 100 l/min. The magnetic drive chemical process pumps are used for chemical pumping as these pumps are corrosion-resistant and energy-efficient, has smooth flow, needs low maintenance, and has size versatility. Similarly, the two peristaltic pumps PT-1 and PT-2 (RH-P120LS and RH-P120S from Ravel Hiteks Pvt. Ltd.) are used for pumping the solutions from the reservoir to the diffusion cell with a certain fixed flow rate to maintain the solution properties (concentration, viscosity, etc.) constant throughout the experimental process. If required, PT-1 and PT-2 can be tuned at a different flow rate to generate a pressure difference. The heating elements (immersion rods) H1 and H2 and temperature sensors S1 and S2 (to monitor the solution temperature) are connected to the temperature control and monitoring unit (TMCU 1 and TMCU 2) in each reservoir (solution-1 and solution-2) as shown in Fig. 1. For the temperature gradient study, one of the heating elements or both can be used to obtain the desired thermal gradient across the membrane. The two diffusion cells are clamped using 2 mm thick silicone sheets having an outer diameter of 25 mm and an inner diameter of 6 mm. The membrane (IEM) under study can be housed between these silicone sheets, or a series of membranes (anion and cation-exchange membranes) can be stacked similarly as reported in Refs. 42–44.

A high current source measurement unit "SMU 2460" procured from Tektronix is connected to record the electrical signals (current or voltage). This SMU has a current range from 50 pA to 7 A and a voltage range from 1 μV to 105 V with extremely low noise and a maximum power rating of 100 W. The "Bio-logic electrochemical instrument" (Bio-logic VSP 300) is used along with the SMU to study the electrochemical impedance spectra and I–V characteristics to perform the ac measurements of the membrane. Similarly, a digital multimeter unit "DMM 6500" procured from Tektronix is connected to record the membrane potential variation with respect to any of the two solutions. The DMM has a current range from 10 pA to 10 A and a voltage range from 100 nV to 1010 V. The SMU and DMM can be replaced based on the specific application. The workstation system is used to operate all the motors [connected via a programmable logic controller

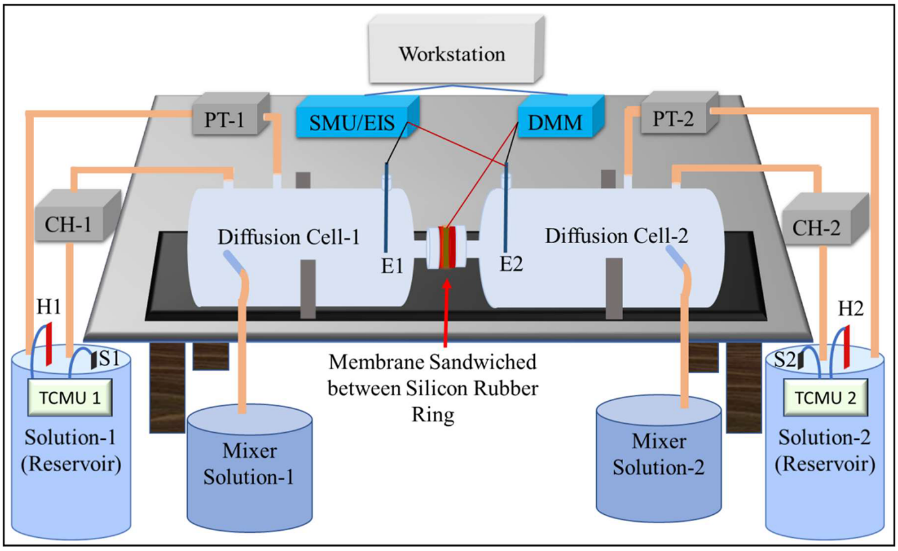

FIG. 1. Schematic of the complete automated experimental setup assembly for the ion transport study using IEMs. The chemical pumps (CH-1 and CH-2) are to pump the solutions from reservoirs to diffusion cells. The peristaltic pumps (PT-1 and PT-2) are to keep rotating the solutions in the diffusion cell at a specified flow rate. The SMU/EIS and DMM are connected to Ag/AgCl electrodes (E1 and E2) for data acquisition. The heating elements (H1 and H2) and heat sensors (S1 and S2) are connected to the temperature control and monitoring unit for temperature monitoring and temperature variation.

Published under an exclusive license by AIP Publishing

(PLC)] and the electrical data acquisition unit (SMU, Bio-logic VSP 300, and DMM) simultaneously, as shown in Fig. 1. "KickStart Instrument" PC control software is to operate the SMU and DMM simultaneously and "ECLab" PC control software for the Bio-logic VSP 300.

The step-by-step assembly of the polycarbonate nanoporous membrane sandwiched between the O-ring-shaped silicon sheets is shown in Fig. 2(a) (the multiple membranes can be stacked similarly). The polycarbonate nanoporous membrane of circular dimension 25 mm is procured from Whatman USA. The silicone sheets hold the membrane in a sandwiched configuration and prevent any chance of leakage when it is clamped between the two diffusion cells. The probing wire is inserted between the silicone sheets to contact the membrane (as shown in Fig. 1) for measuring the membrane potential. The elastic nature of the silicone sheet provides the flexibility to tighten the membrane along with the probe altogether. The schematic of a typical customized diffusion cell is shown in Fig. 2(b) with its dimensions. The cylindrical-shaped diffusion cells are molded with borosilicate glass. Among the top three nozzles of each diffusion cell, the first two fill the solution through the chemical and peristaltic pumps and the third near the neck is to place the electrode. The fourth nozzle drains the solution from the diffusion cells. The neck of the two diffusion cells is molded to hold the sandwiched membrane with the diffusion cells by clamping, as shown in Fig. 1.

III. INSTRUMENTATION AND AUTOMATION

The block diagram in Fig. 3 shows the complete controller unit used to automate the whole setup. The PLC unit "ILC 131 ETH 2700973" procured from Phoenix Contact is used. The PLC is powered with a switching mode power supply (SMPS) "SPB-06-24" procured from Autonics. The PLC is connected to the touch panel display module "BTP 2043W-1050387" procured from Phoenix Contact. The wireless router communicates between the PLC and the personal computer (PC). A dedicated graphical user interface (GUI) (shown in Fig. 4) is designed to interface the PLC with the workstation. The instrument can be operated from any remote location using the PLC IP address (password protected). The operational command is provided through the GUI of the workstation connected to the PLC via the wireless router. Based on the received command, the PLC executes the switching operation and turns on/off the respective relays connected to the three-phase chemical pumps (CH-1 and CH-2) and peristaltic pumps (PT-1 and PT-2).

The GUI is designed to operate the manual and auto mode motors to control the pumps. All four pumps can be operated individually in manual mode, whereas in auto mode, they are operated as per the user-specific application. The auto mode allows the timely synchronization of the motors at the desired flow rate. The PLC offers the flexibility to recalibrate the flow rate for different tube

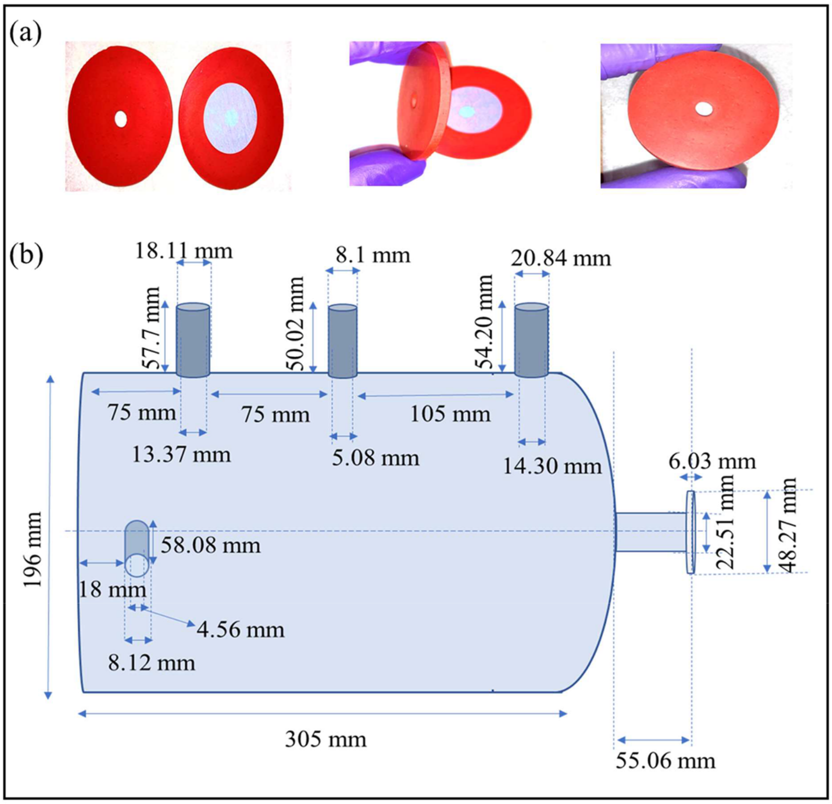

FIG. 2. (a) Step-by-step assembly of the polycarbonate nanoporous membrane for ion transport measurements. (b) Schematic of a single customized diffusion cell of dimension 305 mm length and 196 mm height. The position and dimensions of the nozzles are mentioned. The first two nozzles are for filling the solution through the chemical and peristaltic pumps, and the third nozzle near the neck is to place the electrode. The fourth nozzle drains the solution from the diffusion cells.

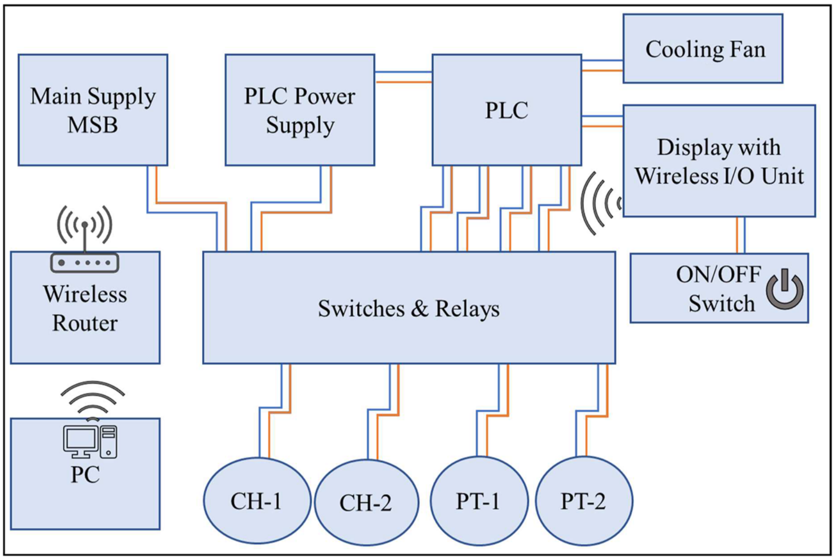

FIG. 3. Controller block diagram with all the input and output interfaces configured to automate the experimental setup. The chemical pumps (CH-1 and CH-2) and peristaltic pumps (PT-1 and PT-2) are controlled through the PLC-controlled relays as per the instructions provided by the user.

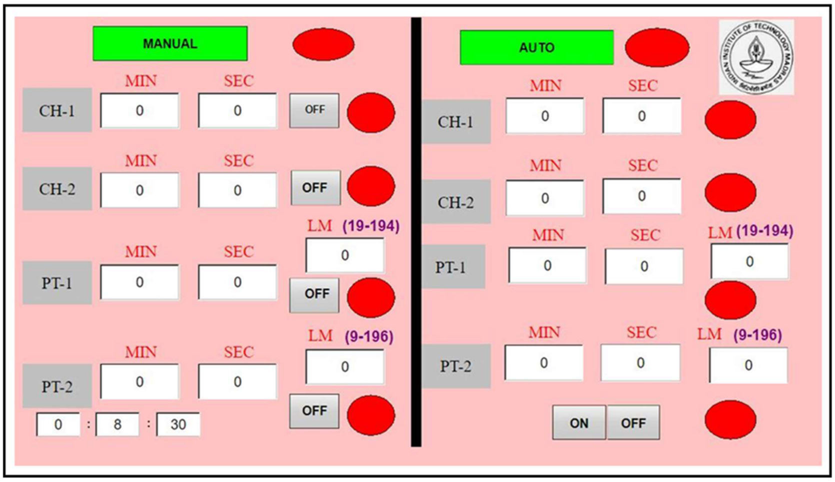

FIG. 4. Graphical user interface of the controller with manual and auto mode options. Both modes have customized flow rates and run-time options for chemical pumps (CH-1 and CH-2) and peristaltic pumps (PT-1 and PT-2).

diameters and peristaltic pumps. The corresponding change will automatically appear in the GUI. The calibration of the instrument is given in Sec. IV.

IV. CALIBRATION OF THE SETUP

Among all used components in the experimental setup, the SMU and DMM are pre-calibrated (as the manufacturer offers the automatic calibration), whereas the calibration of the diffusion cell and pump is performed as follows.

A. Diffusion cell calibration

Figure 5 shows the two conditions that are used to calibrate the flow rate. In one condition, it is assumed that there is a specific flow rate required through the membrane (typically due to applied pressure from one side). In contrast, in the second condition, the flow rate through the membrane is kept at zero with the assumption that only the diffusion or ion-exchange phenomena occur through the membrane. The previous two conditions can be taken together for any desired application and recalibrate the flow rate.

Bernoulli's principle is used prominently in fluid dynamics. This energy conservation principle offers the relationship between pressure, density, and velocity.[45] Bernoulli's equation is used to calibrate the fluid velocity at the inlet and outlet nozzles and through the membrane used to choose the appropriate flow rate pump and corresponding tube diameters.

(a) **Condition 1.** Bernoulli's equation to calculate the fluid flow rate through the membrane between point 1 and point 2 in Fig. 5(a),

$$R + \frac{v_1^2}{2g} + \frac{P_1}{\rho_1 g} = \frac{v_2^2}{2g} + \frac{P_2}{\rho_2 g}, \tag{1}$$

where P_1 is the pressure at point 1, ρ_1 is the fluid density of solution-1 (let the density be heavy), g is the acceleration due

Published under an exclusive license by AIP Publishing

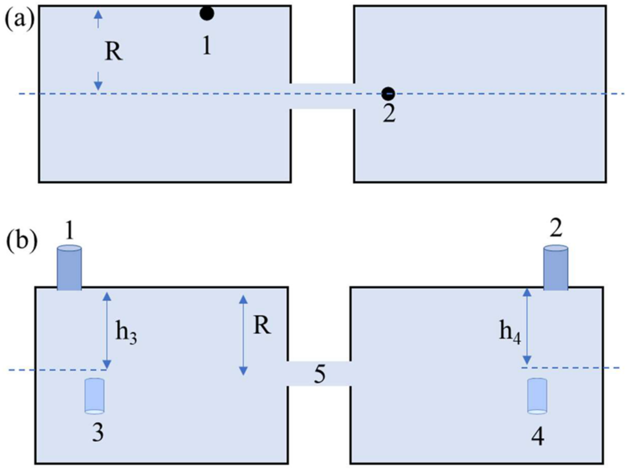

FIG. 5. Schematic of the clamped diffusion cell in the steady-state fluid case to find the flow rate (a) through the membrane and (b) at inlet/outlet nozzles. *R* is the height of fluid from the center of the clamped diffusion cell axis to the top (point 1), and h_3 and h_4 are the heights of the outlet nozzle from inlet nozzle 1 and nozzle 2, respectively.

to gravity, v_1 is the velocity at point 1, P_2 is the pressure at point 2, ρ_2 is the fluid density of solution-2 (let the density be comparatively light), and v_2 is the velocity at point 2,

$$v_1 = 0 \text{ (as it is not moving and staying at the same level).} \tag{2}$$

Using Eqs. (1) and (2), we obtain

$$v_2 = \sqrt{2P_1\left(\frac{1}{\rho_1} - \frac{1}{\rho_2}\right)}. \tag{3}$$

(b) **Condition 2.** Using the continuity equation and Bernoulli's equation to obtain the flow rate from the inlet and outlet nozzles [shown in Fig. 5(b)].

For the left reservoir, we obtain

$$\rho_1 Q_1 - \rho_1 Q_3 - \rho_1 Q_5 = 0. \tag{4}$$

For the right reservoir, we obtain

$$\rho_1 Q_5 - \rho_2 Q_2 - \rho_m Q_4 = 0, \tag{5}$$

where Q_1, Q_2, Q_3, Q_4, and Q_5 are flow rates (m^3/s), A_1, A_2, A_3, and A_4 are the areas of the cross section (m^2), and v_1, v_2, v_3, and v_4 are velocities in the cross section (m/s),

$$Q_1 = A_1 v_1, \tag{6}$$

$$Q_2 = A_2 v_2, \tag{7}$$

$$Q_3 = A_3 v_3, \tag{8}$$

$$Q_4 = A_4 v_4. \tag{9}$$

Applying Bernoulli's equation between point 1 and point 3, we obtain

$$h_3 + \frac{v_1^2}{2g} + \frac{P_1}{\rho_1 g} = \frac{v_3^2}{2g} + \frac{P_3}{\rho_1 g}, \tag{10}$$

$$v_3 = \sqrt{\frac{2(p_1 - p_3)}{\rho_1} + 2gh_3}. \tag{11}$$

Similarly, applying Bernoulli's equation between point 1 and point 3, we obtain

$$h_4 + \frac{v_2^2}{2g} + \frac{P_2}{\rho_2 g} = \frac{v_4^2}{2g} + \frac{P_4}{\rho_m g}, \tag{12}$$

$$v_4 = \sqrt{2\left(\frac{P_2}{\rho_2} - \frac{P_a}{\rho_m} + gh_4\right)}, \tag{13}$$

where ρ_m is the mix solution density and P_3 and $P_4 = P_a$—atmospheric pressure.

B. Peristaltic pump calibration

The flow rate of the peristaltic pump depends on the inner diameter of the tube and the rotation per minute (RPM). As in every revolution, the pumped fluid volume depends on the tube diameter; hence, the tube diameter and volume need to be calibrated first (as in Table I).

TABLE I. Calibrated data for both the peristaltic pumps.

Peristaltic pump 1 (RH-P120S)		Peristaltic pump 2 (RH-P120LS)	
Tube inner diameter	Volume	Tube inner diameter (mm)	Volume (ml)
1 mm	0.15 ml	5	4.5
2 mm	0.4 ml	6	7
3 mm	0.85 ml	8	12
…	…	10	17.5
…	…	12	24

The rotation per minute (RPM) for the required flow rate is calculated as follows:

$$RPM = \frac{Flow\ rate(\mathrm{ml/min})}{\mathrm{ml/revolution}}. \tag{14}$$

For PT-1, the pump head speed variation is between 20 and 196, and for the PT-2 pump, the head speed variation is between 10 and 196. The PLC output voltage is divided to cover the head speed variation of the pump; each variation is experimentally calibrated for the specific flow rate. For every 10 increases in the speed variation number, the PT-1 flow rate increases by 200 ml/min (with a minimum starting flow rate of 200 ml/min), whereas the PT-2 flow rate increases by 30 ml/min (with a minimum flow starting flow rate 30 ml/min).

The SMU and DMM are pre-calibrated by Tektronix. The CH-1 and CH-2 pumps (KE100, KEMS magnetic centrifugal chemical pump) are pre-calibrated for an inlet/outlet inner diameter of 2.5 mm with a maximum head height of 8.2 m at a flow rate of 100 ml/min. It can be noted that the other series of KE XX KEMS magnetic centrifugal chemical pumps can be used based on any specific application for any particular flow rate.

V. ION TRANSPORT MEASUREMENT

The circular polycarbonate membrane of dimension 25 mm and pore size 15 nm is used as an IEM. The membrane is procured from Whatman USA. The monovalent KCl solution is used for this experiment as the ions (K^+ and Cl^-) in this solution have approximately the same hydration size and mobility in water.[46,47] To obtain the concentration gradient (of 1000-fold) across the IEM, one side 0.6 mol and the other side 0.6 mmol KCl solutions are taken. The above experimental setup is used to calculate the salinity gradient energy generation using the ion-selective polycarbonate membrane and show the ion selectivity (t_+) along with the membrane potential (E_m), maximum power (P_{max}), and membrane efficiency (η_{max}) as a case study.

According to Laucirica *et al.*,[48] the membrane potential E_m of the ion-selective nanoporous membrane is given by

$$E_m = (t_+ - t_-)\frac{RT}{F}\ln\left(\frac{\alpha_H}{\alpha_L}\right), \tag{15}$$

where F is Faraday's constant, R is the gas constant, T is temperature (K), t_+ is the cation selectivity, t_- is the anion selectivity, and $t_+ + t_- = 1$.

Hence, the above equation can be written as

$$E_m = (2t_+ - 1)\frac{RT}{F}\ln\left(\frac{\alpha_H}{\alpha_L}\right), \tag{16}$$

where α_H and α_L are the higher and lower concentration activities, respectively. The E_m value of the ion-selective nanoporous membrane depends on the ion selectivity (t_+ and t_-) and salt activity (α_H and α_L). The ion selectivity[49] and the salt activity[50] of the membrane can be expressed as

$$t_+ = \frac{1}{2}\left[1 + \frac{F}{RT}\frac{E_{diff}}{\ln\left(\frac{\alpha_H}{\alpha_L}\right)}\right], \tag{17}$$

where R is the universal gas constant, T is the temperature in Kelvin, F is the Faraday constant, and E_{diff} is the open-circuit voltage obtained from the I–V characteristic plot in Fig. 6(a).

The ionic activities (α_H and α_L) and molalities (m_H and m_L) of the salt solutions are related by the corresponding ionic coefficients (γ_H and γ_L) as

$$\alpha_H = m_H \times \gamma_H, \tag{18}$$

$$\alpha_L = m_L \times \gamma_L, \tag{19}$$

where m_H and m_L are the molal concentrations for higher and lower concentration solutions, and γ_H and γ_L are the activity coefficients for the higher and lower concentration solutions.

The activity coefficient (γ_H and γ_L) can be expressed by the following equation known as the *Debye–Hückel limiting law*:[50]

$$\log \gamma_\pm = -\frac{1.824 \times 10^6}{(\epsilon T)^{3/2}}|Z_+ Z_-|\sqrt{I}, \tag{20}$$

where || denotes the magnitude of the product of valency of the cation and anion, i.e., Z_+Z_-, and the quantity I is the ionic strength given by Gilbert Newton Lewis[50] as

$$I = \frac{1}{2}\sum_i m_i Z_i^2. \tag{21}$$

Equations (16)–(21) are used to calculate the membrane potential (E_m) and the selectivity (t_+) of the ion selectivity nanoporous membrane.

To evaluate and validate the maximum generated osmotic power (P_{max}) and the conversion efficiency (η_{max}) using a salinity gradient from the ion-selective nanoporous polycarbonate membrane, Eqs. (22) and (23) are used.

The maximum power,[49] P_{max}, is given by

$$P_{max} = \frac{I_{oc}E_m}{4}, \tag{22}$$

where I_{oc} is the open-circuit current obtained from the I–V characteristic plot in Fig. 6(a).

The efficiency of the membrane[48] η_{max} is expressed as

$$\eta_{max} = \frac{(2t_+ - 1)^2}{2}. \tag{23}$$

All the above membrane performance parameters mentioned in Table II are calculated using these equations.

The temperature-dependent measurements are performed to ensure that the transport through the membranes is thermally activated hopping.[51] The experiment is performed in isothermal conditions (room temperature) and with a thermal gradient (90 K above room temperature) to validate this study. All the results are shown in Fig. 6(a) and Table II. The results are consistent with those of previously reported work using the same polycarbonate membrane of

Published under an exclusive license by AIP Publishing

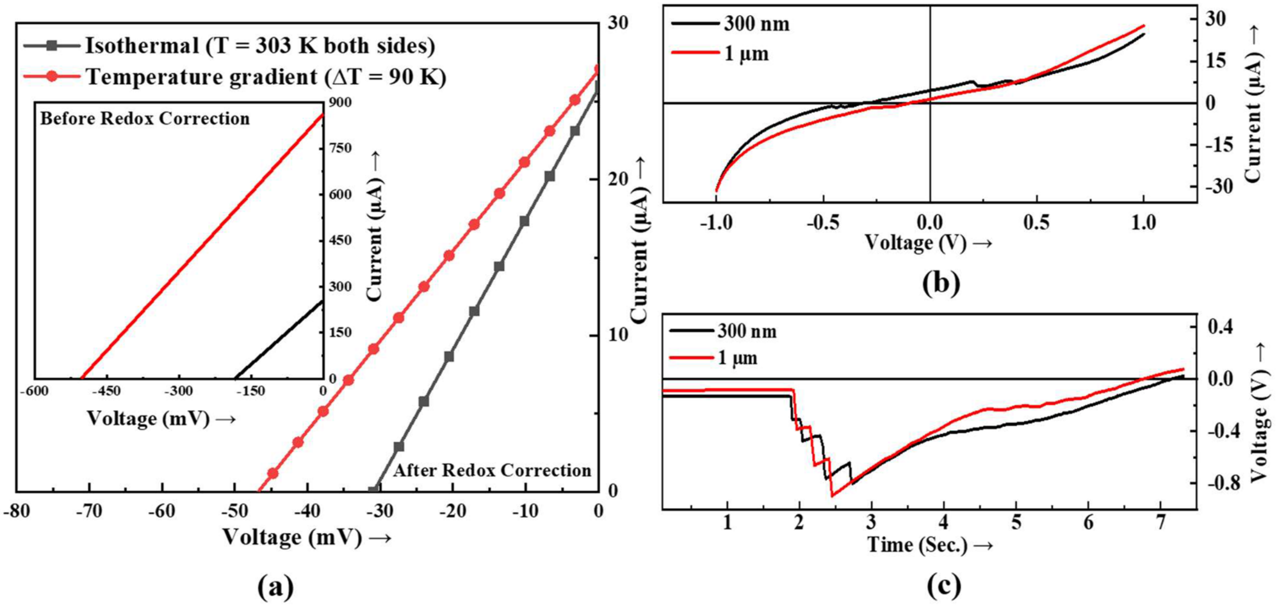

FIG. 6. (a) I–V characteristics of the nanoporous polycarbonate membrane with a 1000-fold concentration gradient in isothermal conditions (303 K on both sides) and with a thermal gradient of 90 K (393 K at the low concentration side and 303 K at the higher concentration side) after the redox correction. The inset displays the I–V characteristics before the redox correction. (b) I–V characteristic plot and (c) corresponding variation in the membrane potential of 300 nm and 1 μm diameter pore Gr/Cu membrane of dimension 10 × 10 mm^2.

the same nanopore dimensions.[51] The lower concentration solution is heated up to boost the power generation of the membrane, similar to that reported earlier.[51]

E_{oc} (open-circuit voltage) and I_{sc} (short circuit current) can be directly obtained from the I–V characteristic plot. E_{oc} includes the combination of both the generated potential (E_{diff}) and redox potential (E_{redox}), which is given by[51]

$$E_{oc} = E_{diff} + E_{redox}. \tag{24}$$

The redox potential (E_{redox}) can be expressed as[52]

$$E_{redox} = \frac{RT}{zF}\log\left(\frac{C_H}{C_L}\right), \tag{25}$$

where z is the valency and C_H and C_L are higher and lower concentration solutions, respectively. After substituting the values of C_H, C_L, z, F, R, and T in Eq. (2), E_{redox} at $\nabla C = 1000$ is estimated to be 153 and 459 mV for 303 and 393 K, respectively. The I–V curves after the redox correction are shown in Fig. 6(a) for isothermal and thermal gradient conditions, and the inset shows the I–V curves before the redox correction.

TABLE II. Membrane performance parameters at isothermal and thermal gradient conditions.

Parameters	Isothermal condition	Thermal gradient
Selectivity (t_+) (%)	60	65
Membrane potential (E_m) (mV)	73.52	110.26
Max power (P_{max}) (nW)	449.53	744.25
Efficiency (η_{max}) (%)	2	4.5

As a case study, the above experimental setup is used to measure the ion transport in the 2D graphene/copper (Gr/Cu) membrane in order to explore one of the applications of ion transport (i.e., salinity gradient energy generation). The Gr/Cu (18 μm thick) membrane of dimension 10 × 10 mm^2 is used as an IEM for the present measurement. The focused ion beam was used to fabricate different pores of diameters 300 nm and 1 μm in Gr/Cu membranes. The I–V characteristic plot of the Gr/Cu membrane is recorded using the above automated experimental setup to calculate energy generation using a salinity gradient [shown in Fig. 6(b)]. Simultaneously, the membrane potential variation is also recorded with respect to the lower concentration solution [shown in Fig. 6(c)]. The short-circuit current and open-circuit voltage are 4.6 μA and 0.27 V for the 300 nm pore and 1.4 μA and 0.09 V for the 1 μm pore, respectively. The estimated power density is 3.44 μW/cm^2 and 0.35 μW/cm^2 for 300 nm and 1 μm pores, respectively.

The impedance measurement is performed in the frequency range of 7 MHz to 150 Hz. At a higher frequency, the Nyquist plot shows a capacitive impedance behavior. The imaginary impedance drops toward zero as the frequency decreases below 2.7 MHz. At a frequency of 21 kHz, the imaginary part of impedance crosses zero and shows positive impedance, which reflects the nature of inductive impedance, as shown in Fig. 7. As described in our earlier work,[53] the multiple arcs in the impedance spectrum are attributed to the

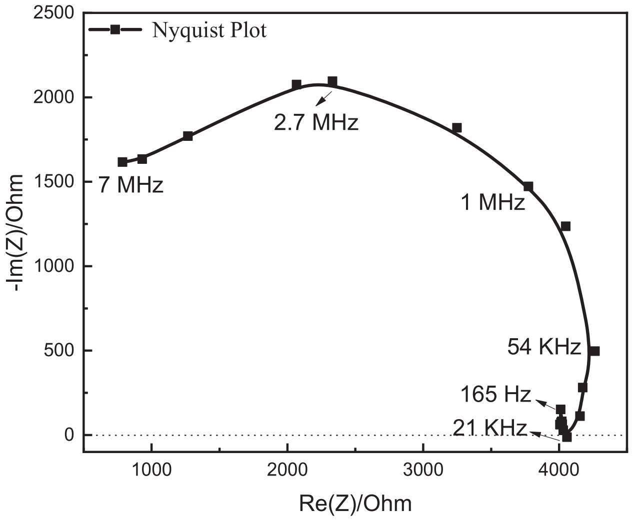

FIG. 7. Impedance spectrum (Nyquist plot) of the nanoporous polycarbonate membrane in the range of 7 MHz to 165 Hz using the automated experimental system.

diffusion transport in the vicinity of the micro/nanochannel interconnect and the effect of ion transport inside the nanochannel. The large hemi circular arc at higher frequencies (Fig. 7) is due to two reasons: (i) the excess ions close to the nanopore surface screen the electrostatic interaction rather than its surface charge density and (ii) the lower frequencies arc shows the inductive characteristics due to the migration of the charges close to the nanopore and bulk interconnect.

VI. CONCLUSION AND OUTLOOK

We have designed and developed an experimental setup for ion transport measurements using ion-exchange membranes. The setup is automated to solve the issues such as controllability, reproducibility, and accuracy and provide reliable ion transport characteristics. All the components in this setup, such as two chemical pumps, two peristaltic pumps, and data acquisition units, are calibrated. A dedicated graphical user interface is designed to interface the PLC with the workstation. The ion transport measurement was performed using an ion-selective polycarbonate nanoporous membrane at room temperature and elevated temperature. The Gr/Cu nano- and microporous membranes were tested for energy harvesting as a case study. The present work will provide a standard tool for realizing reliable ion transport measurements using IEMs. This study can be extended to other membranes with various pore densities, shapes, and sizes for several applications, including reverse electrodialysis, pressure retarded osmosis, fuel cells, redox flow cells, and water desalination.

ACKNOWLEDGMENTS

S.K.Y. thanks Phanendra Kumar for providing support in designing the diffusion cell. V.V.R.N. and P.K.N. acknowledge the financial support from the Ministry of Human Resource Development (MHRD), Government of India (GOI), via the STARS grant [No. STARS/APR2019/148], and the Department of Science and Technology (DST), GOI, via the CRG Grant [No. CRG/2020/001684]. P.K.N. acknowledges the financial support from DST-GoI with sanction Order No. SB/S2/RJN-043/2017 under the Ramanujan Fellowship and support from the Institute of Eminence scheme at IIT-Madras through the 2D Materials Research and Innovation Group. P. K. N. and V.V.R.N. also acknowledge gratefully the support from the Institute of Eminence scheme at IIT-Madras through the Micro Nano-Bio Fluidics Group.

AUTHOR DECLARATIONS

Conflict of Interest

The authors have no conflict to disclose.

Author Contributions

Sharad Kumar Yadav: Conceptualization (equal); Formal analysis (equal); Methodology (equal); Writing – original draft (equal). **Mukesh Kumar:** Formal analysis (equal); Methodology (equal). **Sundara Ramaprabhu:** Investigation (equal); Writing – review & editing (equal). **Vishal V. R. Nandigana:** Conceptualization (equal); Funding acquisition (equal); Supervision (equal); Writing – review & editing (equal). **Pramoda K. Nayak:** Conceptualization (equal); Funding acquisition (equal); Supervision (equal); Writing – review & editing (equal).

DATA AVAILABILITY

The data that support the findings of this study are available from the corresponding author upon reasonable request.

REFERENCES

[1] C. A. Quist-Jensen, F. Macedonio, and E. Drioli, Desalination **364**, 17 (2015).
[2] B. C. H. Steele and A. Heinzel, Nature **414**, 345 (2001).
[3] J. Luo, C. Wu, T. Xu, and Y. Wu, J. Membr. Sci. **366**, 1 (2011).
[4] S. Sarp, Z. Li, and J. Saththasivam, Desalination **389**, 2 (2016).
[5] E. Güler, R. Elizen, D. A. Vermaas, M. Saakes, and K. Nijmeijer, J. Membr. Sci. **446**, 266 (2013).
[6] M.-S. Lee, H.-K. Kim, C.-S. Kim, H.-Y. Suh, K.-S. Nahm, and Y.-W. Choi, ChemistrySelect **2**, 1974 (2017).
[7] J.-Y. Nam, K.-S. Hwang, H.-C. Kim, H. Jeong, H. Kim, E. Jwa, S. Yang, J. Choi, C.-S. Kim, J.-H. Han, and N. Jeong, Water Res. **148**, 261 (2019).
[8] K. Cao, Z. Jiang, X. Zhang, Y. Zhang, J. Zhao, R. Xing, S. Yang, C. Gao, and F. Pan, J. Membr. Sci. **490**, 72 (2015).
[9] S. Lee, H. Kim, and D.-K. Kim, Energies **9**, 49 (2016).
[10] S. H. Kwak, S.-R. Kwon, S. Baek, S.-M. Lim, Y.-C. Joo, and T. D. Chung, Sci. Rep. **6**, 26416 (2016).
[11] W. Xin, Z. Zhang, X. Huang, Y. Hu, T. Zhou, C. Zhu, X.-Y. Kong, L. Jiang, and L. Wen, Nat. Commun. **10**, 3876 (2019).
[12] Z. Zhang, L. He, C. Zhu, Y. Qian, L. Wen, and L. Jiang, Nat. Commun. **11**, 875 (2020).
[13] R. Li, J. Jiang, Q. Liu, Z. Xie, and J. Zhai, Nano Energy **53**, 643 (2018).
[14] X. Liu, M. He, D. Calvani, H. Qi, K. B. S. S. Gupta, H. J. M. de Groot, G. J. A. Sevink, F. Buda, U. Kaiser, and G. F. Schneider, Nat. Nanotechnol. **15**, 307 (2020).
[15] C.-Y. Lin, C. Combs, Y.-S. Su, L.-H. Yeh, and Z. S. Siwy, J. Am. Chem. Soc. **141**, 3691 (2019).
[16] S. Balme, T. Ma, E. Balanzat, and J.-M. Janot, J. Membr. Sci. **544**, 18 (2017).

Published under an exclusive license by AIP Publishing

[17] M. I. Walker, K. Ubych, V. Saraswat, E. A. Chalklen, P. Braeuninger-Weimer, S. Caneva, R. S. Weatherup, S. Hofmann, and U. F. Keyser, ACS Nano **11**, 1340 (2017).

[18] R. C. Rollings, A. T. Kuan, and J. A. Golovchenko, Nat. Commun. **7**, 11408 (2016).

[19] J. Feng, K. Liu, M. Graf, M. Lihter, R. D. Bulushev, D. Dumcenco, D. T. L. Alexander, D. Krasnozhon, T. Vuletic, A. Kis, and A. Radenovic, Nano Lett. **15**, 3431 (2015).

[20] J. Feng, M. Graf, K. Liu, D. Ovchinnikov, D. Dumcenco, M. Heiranian, V. Nandigana, N. R. Aluru, A. Kis, and A. Radenovic, Nature **536**, 197 (2016).

[21] M. Macha, S. Marion, V. V. R. Nandigana, and A. Radenovic, Nat. Rev. Mater. **4**, 588 (2019).

[22] A. Siria, P. Poncharal, A.-L. Biance, R. Fulcrand, X. Blase, S. T. Purcell, and L. Bocquet, Nature **494**, 455 (2013).

[23] H. Cheng, Y. Zhou, Y. Feng, W. Geng, Q. Liu, W. Guo, and L. Jiang, Adv. Mater. **29**, 1700177 (2017).

[24] S. Hong, F. Ming, Y. Shi, R. Li, I. S. Kim, C. Y. Tang, H. N. Alshareef, and P. Wang, ACS Nano **13**, 8917 (2019).

[25] R. E. Pattle, Nature **174**, 660 (1954).

[26] R. S. Norman, Science **186**, 350 (1974).

[27] D. Stein, M. Kruithof, and C. Dekker, Phys. Rev. Lett. **93**, 035901 (2004).

[28] H. Daiguji, P. Yang, and A. Majumdar, Nano Lett. **4**, 137 (2004).

[29] A. Alabi, A. AlHajaj, L. Cseri, G. Szekely, P. Budd, and L. Zou, npj Clean Water **1**, 10 (2018).

[30] Z. S. Siwy, M. R. Powell, E. Kalman, R. D. Astumian, and R. S. Eisenberg, Nano Lett. **6**, 473 (2006).

[31] E. C. Yusko, R. An, and M. Mayer, ACS Nano **4**, 477 (2010).

[32] J. Ji, Q. Kang, Y. Zhou, Y. Feng, X. Chen, J. Yuan, W. Guo, Y. Wei, and L. Jiang, Adv. Funct. Mater. **27**, 1603623 (2017).

[33] C.-Y. Lin, P.-H. Wong, P.-H. Wang, Z. S. Siwy, and L.-H. Yeh, ACS Appl. Mater. Interfaces **12**, 3198 (2020).

[34] S. Park and G. Yossifon, Phys. Rev. E **93**, 062614 (2016).

[35] Y. Qiu, R. A. Lucas, and Z. S. Siwy, J. Phys. Chem. Lett. **8**, 3846 (2017).

[36] X. He, K. Zhang, T. Li, Y. Jiang, P. Yu, and L. Mao, J. Am. Chem. Soc. **139**, 1396 (2017).

[37] M. Gao, P. C. Tsai, Y. S. Su, P. H. Peng, and L. H. Yeh, Small **16**, 2006013 (2020).

[38] R. A. Lucas, C.-Y. Lin, and Z. S. Siwy, J. Phys. Chem. B **123**, 6123 (2019).

[39] A. Szczesny, P. Śniecikowski, J. Szmidt, and A. Werbowy, Vacuum **70**, 249 (2003).

[40] A. Achilli, T. Y. Cath, and A. E. Childress, J. Membr. Sci. **343**, 42 (2009).

[41] J. W. Post, H. V. M. Hamelers, and C. J. N. Buisman, Environ. Sci. Technol. **42**, 5785 (2008).

[42] J. Chen, W. Xin, X.-Y. Kong, Y. Qian, X. Zhao, W. Chen, Y. Sun, Y. Wu, L. Jiang, and L. Wen, ACS Energy Lett. **5**, 742 (2020).

[43] G. Z. Ramon, B. J. Feinberg, and E. M. V. Hoek, Energy Environ. Sci. **4**, 4423 (2011).

[44] D.-C. Zheng and L.-H. Yeh, Micromachines **11**, 949 (2020).

[45] *Handbook of Valves and Actuators*, edited by B. Nesbitt (Butterworth-Heinemann, Oxford, 2007), pp. 43–79.

[46] R. W. Impey, P. A. Madden, and I. R. McDonald, J. Phys. Chem. **87**, 5071 (1983).

[47] J. N. Israelachvili, *Intermolecular and Surface Forces*, 3rd ed. (Academic Press, San Diego, 2011), pp. 71–90.

[48] G. Laucirica, M. E. Toimil-Molares, C. Trautmann, W. Marmisollé, and O. Azzaroni, Chem. Sci. **12**, 12874 (2021).

[49] M. H. Ali Haider, S. Nasir, M. Ali, P. Ramirez, J. Cervera, S. Mafe, and W. Ensinger, Mater. Today Energy **23**, 100909 (2022).

[50] J. Zimmerman, Biochem. Mol. Biol. Educ. **33**, 382 (2005).

[51] V.-P. Mai and R.-J. Yang, Appl. Energy **274**, 115294 (2020).

[52] B. Alexander Yi and L. Y. Jan, *Encyclopedia of the Human Brain*, edited by V. S. Ramachandran (Academic Press, New York, 2002), pp. 599–615.

[53] V. V. R. Nandigana and N. R. Aluru, Electrochim. Acta **105**, 514 (2013).

Published under an exclusive license by AIP Publishing